Effect of Molybdenum on Ductility Dip Cracking in Nickel-Base Weld Filler Metal 52XL

Undergraduate Thesis

Presented in Partial Fulfillment of the Requirements for Graduation with Research Distinction in the College of Engineering of The Ohio State University

By

Stan Blados

Welding Engineering Program

The Ohio State University

2018

Defense Committee

Carolin Fink, Dr.-Ing, Advisor

John C. Lippold, Prof.

Abstract

The nuclear industry has an increasing demand for thick cross-section walls from nickel-based alloys for structural and repair applications. Due to the high restraint and residual stresses developing in these welds, ductility dip cracking (DDC) is a major problem, especially when using high chromium nickel-based filler metals. Previous research has shown that alloying elements, such as niobium (Nb) and tantalum (Ta) decrease the susceptibility to DDC by the formation of eutectic carbides along the solidification grain boundaries. These carbides pin the grain boundaries in the weld metal, which results in tortuous grain boundaries causing a mechanical locking effect, so that DDC formation by grain boundary sliding is mitigated.

The objective of this undergraduate research is to determine the effect of molybdenum (Mo) on DDC in nickel based Ta-bearing FM 52XL. Mo is an alloying element in nickel-based alloys to increase high temperature strength. The influence of Mo on DDC is not well understood, and contradictory results have been reported. Microstructural characterization was done on weldability samples with different Mo content to evaluate the effect on eutectic formation, grain size, tortuosity, grain boundary precipitates and hardness. Image analysis on light optical micrographs (LOM) and scanning electron micrographs (SEM) was used to determine the amount of eutectic in the weld metal and the weld metal grain size as a function of the Mo content. Results with the LOM showed no conclusive correlation, but the SEM images showed an increased amount of eutectic with Mo additions. Grain size measurements have shown that the Mo bearing weld metal exhibits a finer grain structure. Tortuosity measurements show that the sample without Mo has the highest curvature but the lowest DDC resistance, this could indicate that there could be other factors that increase DDC resistance in FM 52XL. $M_{23}C_6$ precipitates were found to be continuous along the grain boundaries, and were noticed to be coarser in the variant without Mo. Hardness measurements determined that both Mo and Ta have a solid-solution strengthening effect in FM 52XL.

Acknowledgments

I would like to thank my research advisor, Carolin Fink, for a great amount of help, support and guidance on this project. I would like to also thank Louie Aguilar for help working with the different features of MIPAR. And I would like to thank Luke Johnson for his help with the SEM images.

Table of Contents

List of Tables

List of Figures

Chapter 1. Introduction

The nuclear industry had to reengineer old nuclear power plants because cracking had been noticed after 40 years of service in the nickel-base alloys. To mitigate this type of cracking higher chromium (~30%) nickel-base alloys replaced the ones previously used (~15%). High restraints and multi pass weld setups led to ductility dip cracking (DDC) issues in these high chromium nickel-base alloys, and a need to develop DDC resistant filler metals for welding of thick cross-section components in nuclear power plants. The additions of niobium (Nb) decreased DDC susceptibility by creating tortuous grain boundaries in the weld metal, which results in less grain boundary sliding and hence mitigates crack initiation due to mechanical locking. However, with the addition of niobium the solidification temperature range increased causing an increase in solidification cracking susceptibility. Recently, to combat solidification cracking tantalum (Ta) was used to replace niobium, and has been shown to provide both resistance to DDC and solidification cracking. Different addition of tantalum and molybdenum (Mo) were used during the development of this new filler metal. Molybdenum is added to nickel-base filler metals to increase solid-solution strengthening. Molybdenum seems to also add to an increased DDC resistance in the Ta containing filler metals. But at this point it is not clear what the specific effect of molybdenum is in terms of DDC resistance.

This research was conducted to determine what the addition of molybdenum does in the weld metal microstructure that could cause an increase in DDC resistance. This study investigated if molybdenum contributes to the phases that form at the end of solidification or changes the amount of eutectic phase. Also, grain boundary tortuosity and grain size were evaluated as a function of Mo and Ta additions. The study looked at differences in precipitation along grain boundaries, which could impact DDC resistance as a grain boundary sliding phenomena. Lastly, the solid-solution effect of Mo and Ta was evaluated using hardness measurements.

Chapter 2: Background

2.1 Use of High-Chromium Nickel-Base Filler Metals in the Nuclear Industry

The nuclear industry has been using Alloy 600 for many years due to its good high temperature properties. However, 40 years after fabrication, cracking was discovered during inspection of these parts and was identified as primary water stress corrosion cracking (PWSCC) [1]. This type of cracking occurs in a primary water environment with high tensile stresses and is related to intergranular stress corrosion cracking.

To mitigate PWSCC, Alloy 690 was used instead of Alloy 600, because it has a higher amount of chromium (30 wt.-%) that increases its corrosion resistance compared to Alloy 600 (15 wt.-% Chromium). The matching filler metals for alloy 600 and alloy 690 are filler metal (FM) 82 and FM 52 respectively. [2] These FMs have similar properties to their base metal in terms of corrosion resistance.

Alloy 690 was used with FM 52 extensively in the nuclear industry and a new issue was encountered in welds, ductility dip cracking (DDC). This new issue was mitigated by the addition of niobium (Nb) to the FM, which caused the grain boundaries to be tortuous, locked grain boundary sliding and hence mitigated DDC. This will be discussed later in section 2.3.1. When niobium was added to FM 52 the weld became

susceptible to solidification cracking [3]. This was mitigated by replacing the Nb with tantalum (Ta). Addition of Ta decreases the solidification temperature range (STR) and made the FM less susceptible to solidification cracking [4].

2.2 Effect of Alloying Elements in High-Chromium Nickel-base Filler Metals

There are different alloying elements that can be used in high-Cr Ni base FMs, including: Cr, Nb, Ta, and molybdenum (Mo). As mentioned earlier, Cr is added to Ni base alloys to reduce the susceptibility to corrosion, and for FM 52 it was added to specifically reduce the susceptibility to PWSCC. Nb is added to form MC carbides that form at the end of solidification in a eutectic reaction. These carbides pin the grain boundaries from migrating, which results in more tortuous grain boundaries and therefore inhibits grain boundary sliding and reduces the susceptibility to DDC [5]. Similarly, to Nb, Ta form a eutectic at the end of solidification, and it has been shown to provide resistance to solidification cracking [4]. Ta- and Nb- bearing filler metal samples were evaluated by Fink et al. [4] in the cast pin tear test (CPTT) to determine solidification cracking resistance. The results are shown in Figure 1. It was determined that the Nb-bearing FM52 MSS-C was the most susceptible to solidification cracking whereas Ta-bearing type 52M filler metals had higher cracking resistance.

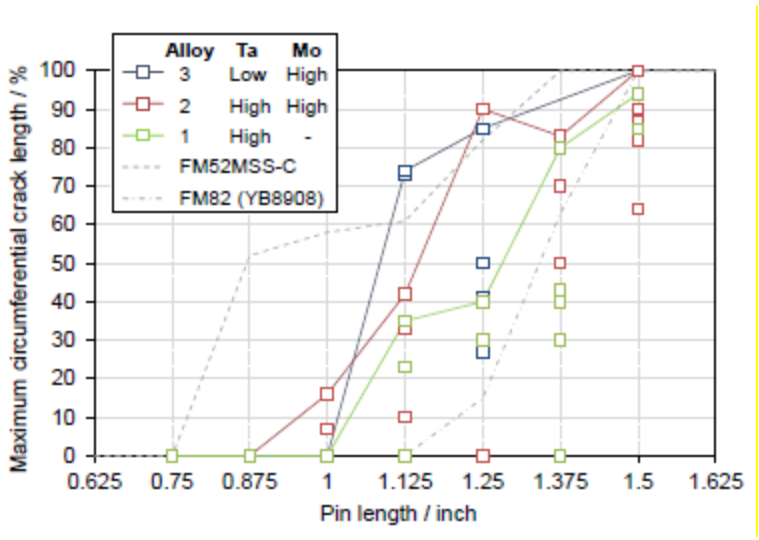

Figure 1: Cast pin tear test (CPTT) results for FM52M with additions of Ta and Mo [4]

It has been previously shown that the addition of Mo to high-Chromium Nickel-base FM reduces the susceptibility of DDC. When added to a Nb-bearing FM it reduces the susceptibility to DDC when compared to a filler metal with no Mo additions. $M_{23}C_6$ precipitates have been found along the grain boundaries of high-Chromium Nickel-base alloys, as seen in Figure 2 [6]. The M element for these precipitates is typically chromium (Cr), but Mo can substitute for some of the Cr in Mo-bearing alloys.

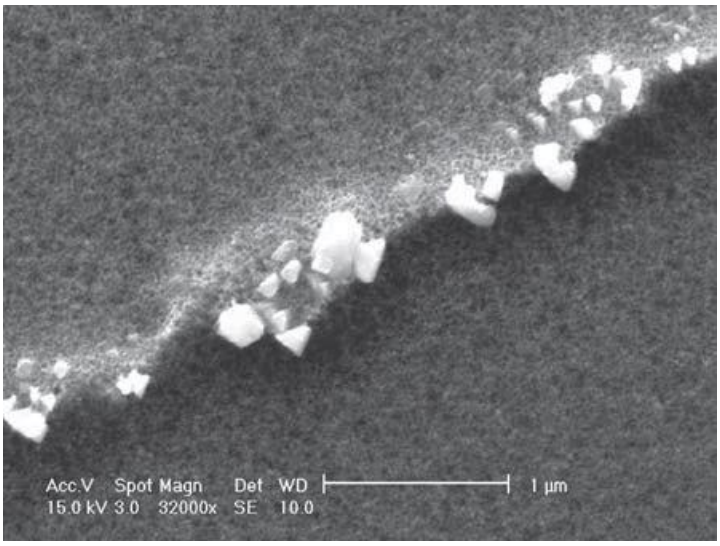

Figure 2: $M_{23}C_6$ precipitates on a grain boundary of high chromium Ni-base weld metal [6]

The addition of Mo (up to 6 wt.%) to Nickel-base FM was also studied by Zhang et al. [7]. The authors determined that the more Mo was added to the FM, the lower the impact energy (Charpy toughness) of the weld metal, as shown in Figure 3. Zhang et al. [7] claimed that as the amounts of Nb and Mo increases, the eutectic precipitates become larger and Laves phase forms at higher than 4 wt% Mo in the weld microstructure, thus lowering the impact strength, as seen in Figure 3. The authors also state that Nb and Mo create a solid-strengthening effect in the weld metal, which causes its ultimate tensile strength to go up with increasing alloy content.

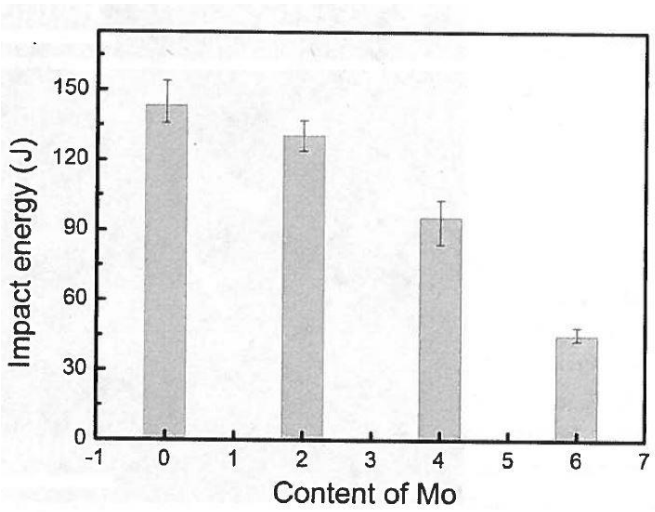

Figure 3: The effect of Mo additions on impact energy of high-chromium nickel-base alloys [7]

Fink et al. [4] used hardness measurements to determine the solid-solution strengthening effects of Ta and Mo in a newly developed Ta- and Mo- bearing FM 52M-type filler metal (52XL). They showed that Mo has a solid strengthening effect while Ta does not add as much strength, see Figure 4. It was also reported that compositions with high Ta and high Mo (4 wt.-%) have a higher resistance to DDC due to the more tortuous boundaries than high Ta-bearing composition with no Mo and alloys with low Ta (2 wt.-%) and high Mo (4 wt.-%) that have straighter grain boundaries.

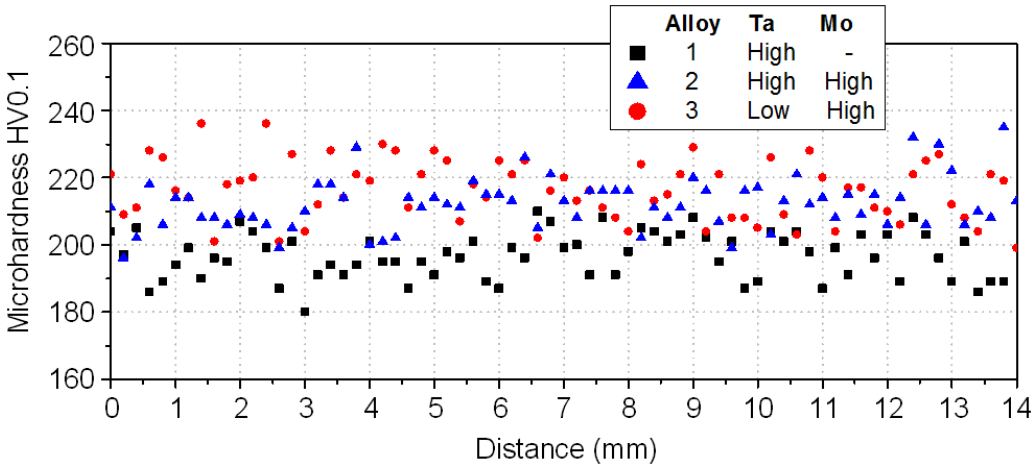

Figure 4: Hardness traverse across cast pin samples of Ta and Mo-bearing 52XL variants [4].

In high-Cr nickel-base alloys the effect of Nb plays a role for the fraction eutectic (F_E) that forms at the end of solidification. In Table 1, there is the measured amount of F_E as determined in a study by Wheeling and Lippold [8]. The more Nb was added to the weld metal the more F_E formed. At high amounts of Nb, it was shows that there is a significant decrease in solidification cracking resistance. This is due to backfilling that occurs at high amounts of eutectic liquid. According to Wheeling and Lippold [8], addition of Mo did not change the amount of F_E, as seen in Table 1.

Table 1: Compositions of alloys and the measured and calculated fraction eutectic [8].

Composition	k_{Nb}	k_{Mo}	Calculated F_E ($f_s = 0.95$)	Calculated F_E ($f_s = 0.98$)	Measured vol. F_E	Avg. final wt. fraction Nb	Avg. final wt. fraction Mo
Alloy 690	0.16	–	–	–	0.003 ± 0.001	–	–
2Nb0Mo	0.17	–	0.00448	0.025522	0.014 ± 0.006	0.201	–
2Nb2Mo	0.17	0.66	0.00319	0.026811	–	0.191	0.0656
2Nb4Mo	0.17	0.68	0.00129	0.028708	–	0.183	0.118
4Nb0Mo	0.18	–	0.065893	0.095893	0.075 ± 0.01	0.217	–
4Nb2Mo	0.18	0.67	0.068589	0.098589	–	0.206	0.0700
4Nb4Mo	0.18	0.69	0.072664	0.102664	–	0.199	0.124
6Nb0Mo	0.19	–	0.15167	0.18167	0.144 ± 0.03	0.223	–
6Nb2Mo	0.19	0.68	0.156274	0.186274	–	0.212	0.0736
6Nb4Mo	0.19	0.69	0.160404	0.190404	–	0.204	0.129
8Nb0Mo	0.20	–	0.25281	0.28281	0.239 ± 0.018	0.227	–

Wheeling and Lippold [9] used the Hot Ductility Test to look at the effect of varying amounts of Nb and Mo. They measured the reduction in area (RA) of their samples at different test temperatures. The results in Table 2 showed that there was no statistically significant difference in the samples, except an outlier of the 4Nb0Mo composition that at 1200 °C had a high reduction in area (RA) of 17%. All other samples were very close to zero RA. From extensive fractography at the fracture surfaces, it was found that there were more liquid films at lower temperatures in the samples with Mo additions as compared to the samples with no Mo. It was hypothesized that Mo promotes solidification crack healing, though the specific reason is not yet understood.

Table 2: Hot ductility tests results with additions of Nb and Mo [9].

Condition	Composition	Reduction in Area (%)
6 s at 1200 °C	4Nb0Mo	17
	4Nb6Mo	0
	6Nb0Mo	2
	6Nb4Mo	0
6 s at 1250 °C	4Nb0Mo	3
	4Nb6Mo	0
	6Nb0Mo	1
	6Nb4Mo	0

2.3 Ductility Dip Cracking

Ductility Dip Cracking (DDC) gets its name from a dip in ductility that occurs in nickel-base alloys, austenitic stainless steels, Aluminum alloys, Copper alloys and Titanium alloys. The commonality in these metals is that they all have a close packed crystallographic orientation of face centered cubic (FCC), apart from Titanium alloys that are hexagonally close packed (HCP). This dip in ductility happens between 0.5 and 0.8 of the melting temperature (T_m). A schematic of the ductility dip can be seen in Figure 5. In Figure 5, a normal ductility signature is shown where ductility increases with increasing temperature (the black curve), but for alloys susceptible to DDC, the ductility drops in an intermediate temperature range, called ductility dip temperature range (DTR).

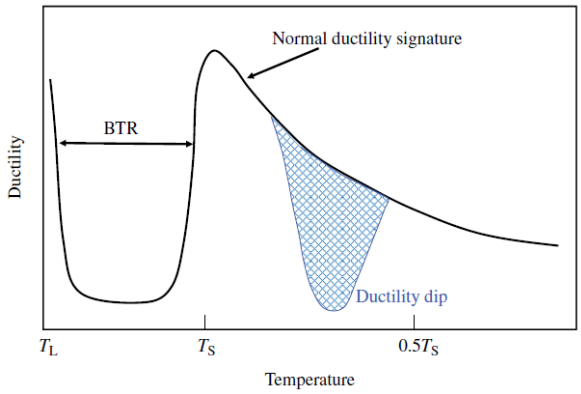

Figure 5: Ductility dip schematic [10]

DDC is not a new phenomenon, it has been seen since 1912 and has been reported in 1961 to occur due to a ductility dip in FCC alloys [11]. This cracking phenomenon was often mislabeled as solidification cracking and/or different terminology was used, including intermediate temperature embrittlement, and microfissuring. DDC always occurs intergranularly (IG), i.e. along grain boundaries.

DDC occurs in multi pass welds in reheated nickel-base weld metal. This is because for DDC to occur, the weld metal needs to go through a thermal cycle that passes it through the DTR at the same time as there is high restraint present. During multi pass welding high residual stresses are build-up and continue to increase as subsequent passes are overlaid. Each pass creates a thermal cycle in the weld metal if the previous pass is subjecting it to temperatures within the ductility dip temperature range (DTR). A low the ductility in the DTR and high restraint levels lead to DDC in susceptible materials, such as some nickel-base filler metals.

2.3.1 Mechanisms of DDC

There are many theories on the mechanisms of the DDC phenomenon. The proposed mechanisms were summarized by Lippold et al. [10], seen in Table 3.

Table 3: Ductility dip cracking theories [10]

Name	Description	Year
Rhines and Wray [2]	Grain boundary shearing up to recrystallization temperature	1961
Yamaguchi *et al*. [11]	Sulfur segregation and embrittlement	1979
Zhang *et al*. [12, 13]	Combination of effects up to recrystallization temperature	1985
Ramirez and Lippold [14, 15]	Grain boundary sliding, microvoid formation, boundary tortuosity	2004
Nishimoto *et al*. [16–18]	Impurity segregation	2006
Noecker II and DuPont [19, 20]	Grain boundary sliding, carbide distribution and morphology	2007
Young *et al*. [21]	Precipitation-induced cracking	2008

Early mechanisms, by Rhines and Wray [12], stated that dynamic recrystallization was a cause of DDC. Dynamic recrystallization is a phenomenon that occurs when the material is strained and subjected to high temperatures at the same time. At locations of high stress concentration, such as grain boundary triple points, new grains form as seen in Figure 6.

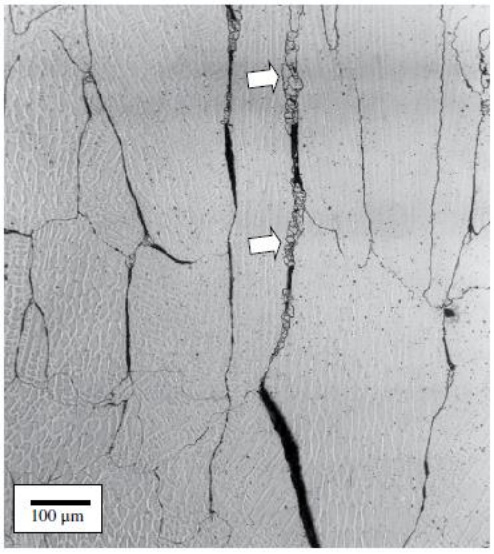

Figure 6: Micrograph of a DDC, arrows indicate dynamic recrystallization [12]

The agreed upon mechanism for DDC by most researchers is that it is a grain boundary sliding phenomenon [13-14]. Grain boundary sliding causes stresses on the grain boundary triple points in the weld metal microstructure. Void form off these triple points and continue into DDC. The stress concentration on grain boundary triple points can be reduced by increasing the grain boundary tortuosity of the weld metal. This tortuosity decentralizes the stresses and creates a mechanical locking that mitigates grain boundary sliding, seen in Figure 7. Another way, also depicted in Figure 7, is to reduce grain boundary sliding by having precipitates along the grain boundaries. These precipitates also serve as a locking mechanism that inhibits grain boundary sliding and reduces stress concentration at triple points.

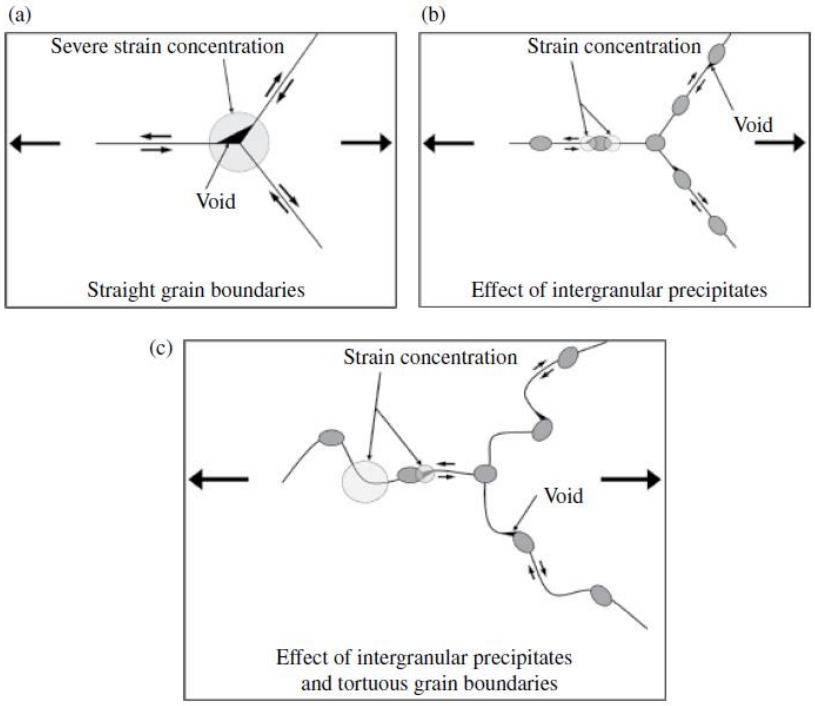

Figure 7: Schematics of DDC initiation, (a) formation at triple points, (b) formation at precipitates, (c) tortuosity and precipitates impede void formation [13]

Sulfur has been determined to increase the susceptibility to DDC. This is believed to be due to the fact that it segregates to the grain boundaries causing embrittlement. Collins et al. [15] states that Sulfur is only a factor and not a cause of DDC, because DDC was also reported in high purity alloys, where the Sulfur contents is extremely low. Hydrogen is another factor that increases susceptibility to DDC. Work done by Collins et al. [16] added 2% Hydrogen to the shielding gas in the strain-to-fracture samples causing more DDC to occur.

Grain size plays an important role on DDC and controlling grain size can help reduce the susceptibility to DDC. This is because DDC is a grain boundary sliding phenomenon and cracking occurs due to strain build up along the grain boundaries. The

larger the grains the less grain boundary area there is. This means in a larger grain structure; the strain is more localized at a single grain boundary thus cracking occurs easier. While with smaller grains, there is more overall grain boundary area, strains are more distributed and the material is less likely to crack [17].

2.3.2 DDC in High Chromium Nickel-based Alloys

The increase of chromium between Alloy 600 and Alloy 690 eliminates the susceptibility to PWSCC but increased the susceptibility to DDC [15]. The matching filler metal for Alloy 690 is filler metal (FM) 52 and this FM has different properties than the FM used for Alloy 600, FM 82. The change to a higher chromium alloy made FM 52 more likely to form straight grain boundaries. This was because the FM 82 formed MC (eutectic carbides) while there was no consistent formation of MC in FM 52 [16].

New alloys of FM 52 were created to mitigate DDC. These new alloys FM 52M contain ~1% Nb and FM 52MSS contained 2.5% Nb and 4% Mo. In FM 52M niobium was added to from NbC that would pin the grain boundaries to make them tortuous (as described in earlier section). This small addition of niobium was only slightly helpful in reducing DDC, as shown in Figure 8. The FM 52MSS had niobium to form the MC carbides but it also had additions of Mo, the additions of Mo greatly reduced the cracking susceptibility to DDC, as shown in Figure 8 [16].

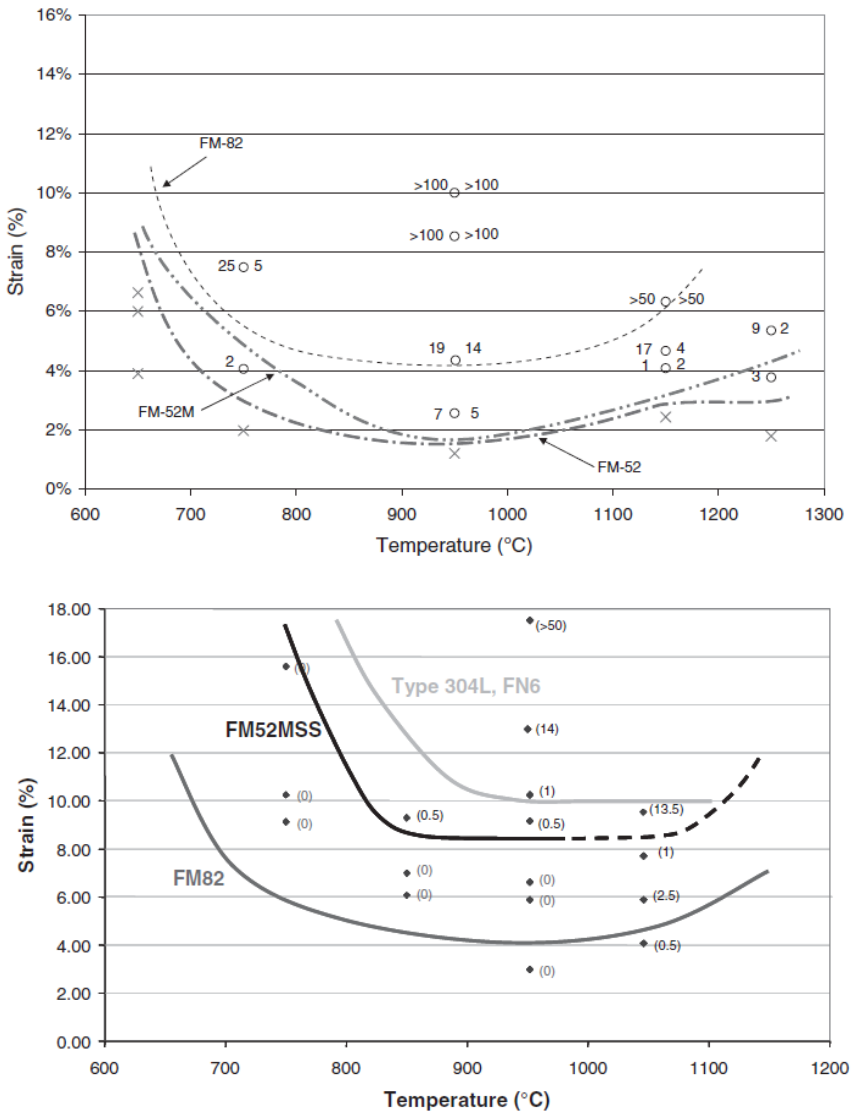

Figure 8: STF test results: Comparison of FM52, FM52M, and FM82 (top), and a comparison of FM82, FM52MSS, and Type 304L stainless steel (bottom) [6].

There are two reasons why FM 52MSS greatly reduced susceptibility to DDC. One is because the Nb that was added formed NbC which formed at the end of solidification and pinned the grain boundaries. This pinning made the grain boundaries tortuous. This tortuosity created a mechanical locking that inhibited grain boundary

sliding and therefore DDC. There is also the addition of Mo that forms $M_{23}C_6$, it is uncertain whether this precipitate helps mitigate DDC, or if Mo contributes to some other effect. Noecker and DuPont [2] hypothesized that there is a localized stress that can form at the grain boundary carbide interface locking the boundary.

Young et al. [18] proposed in his work, that $(Fe,Cr)_{23}C_6$ carbides are a major contributor to DDC this is because they from localized solidification stresses upon cooling. The authors also state that additions of Nb or Ti form MC carbides and reduce the formation of $(Fe,Cr)_{23}C_6$. He claims that DDC is a precipitation cracking mechanism. Though this is not always true because nickel alloys can be susceptible to DDC even when there are no carbides/precipitates.

There is a strong relationship between the brittle temperature range (BTR) and the ductility dip temperature range (DTR), shown in Figure 5. The BTR determines solidification cracking susceptibility. Additions of Nb increase the solidification temperature range of the FM 52MSS alloy as compared to the FM 52 alloy. To combat this change, other elements that had similar properties to Nb, such as Ta and Hf, were used to replace Nb [19]. The idea was to reduce solidification cracking while keeping high DDC resistance. Hf was ruled out due to having very low resistance to solidification cracking in the cast pin tear test. Additions of tantalum increased the resistance to solidification cracking, and STF testing also showed that the DDC resistance is high and similar to FM 52MSS, as seen in Figure 9.

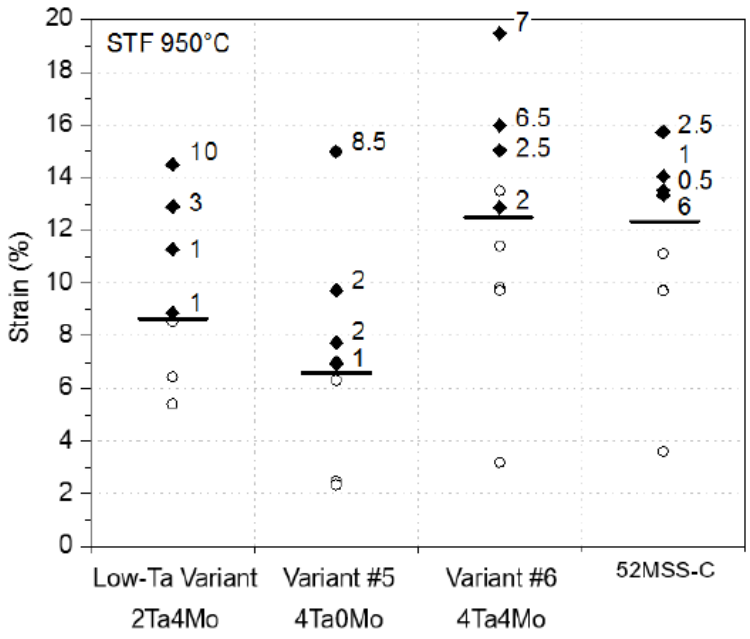

Figure 9: STF test results for FM52XL with Ta and Mo additions [4]

Chapter 3: Objectives

The overall objective of this research is to determine the effect of molybdenum on ductility dip cracking (DDC) in nickel-base filler metal 52XL. This will be achieved by pursuing the following specific goals:

1. Summarize the current knowledge/available literature on the effect of molybdenum additions on DDC susceptibility in high chromium nickel-base filler metals.

2. Determine the effect of molybdenum additions on the amount of eutectic phase formation at the end of weld solidification in Nb- and Ta-bearing high-Cr nickel-base filler metals.

3. Determine the effect of molybdenum additions on grain size and grain boundary tortuosity in the weld metal microstructure of Ta-bearing high-Cr nickel-base filler metals.

4. Identify the role of molybdenum in the (eutectic) phase formation during weld solidification of Ta-bearing high-Cr nickel-base filler metals.

5. Determine the effect of molybdenum as a solid-solution strengthening element on the DDC susceptibility of Ta-bearing high-Cr nickel-base filler metals.

Chapter 4: Experimental Procedures

4.1 Materials

This study considers the characterization of three Ni-30Cr filler metals derived from FM 52 with additions of tantalum (Ta) and/or molybdenum (Mo). The different variants contain amounts of tantalum that forms carbides (TaC) at the end of solidification in a eutectic reaction [4]. These carbides pin the grain boundaries, which results in more tortuous grain boundaries in the deposited weld metal and helps to prevent DDC. Two of the filler metals contain molybdenum, which is added to this material for solid-solution strengthening to improve high temperature strength. The chemical compositions of the three filler metal variants are listed below in Table 4. All variants are within the composition tolerances of AWS A5.14 ERNiCrFe-13 (FM 52MSS) [4].

Table 4: Compositions of samples (in wt.-%)

Filler Metal	Nominal	Ni	Cr	Fe	Mo	Ta	C	Al	Ti
Variant #4/6	2Ta4Mo	Bal.	29.705	8.13	3.845	1.911	0.035	0.012	0.0025
Variant #5	4Ta0Mo	Bal.	29.83	7.99	<0.005	3.88	0.035	0.007	0.004
Variant #6	4Ta4Mo	Bal.	29.76	8.05	3.86	3.82	0.033	0.01	0.003
ErNiCrFe-13 (AWS 5.14)		52-62	28.5-31	Bal.	3.0-5.0	2.1-4.0	0.03	0.50	0.50

The filler metal samples that were analyzed in this study were samples of two different weldability tests, i.e. the cast pin tear test (CPTT), and the strain-to-fracture test (STF) that were previously performed on the three filler metal variants [4]. Additional samples were prepared in an arc melting system that consists of a gas tungsten arc (GTA) torch, which melts the samples in to "buttons" (button-shaped samples) in a controlled argon environment in a water cooled copper crucible (Figure 10). The buttons where prepared at a weight of 12.5 grams using arc-melting of welding wire with the compositions listed in Table 4.

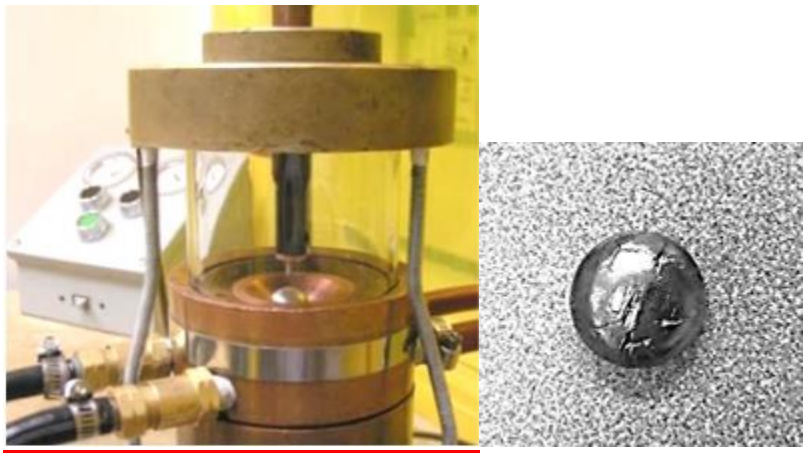

Figure 10: Button arc-melting device at The Ohio State University [20] (left), and an arc melted button shaped sample (right).

The cast pin samples were made in the cast pin tear testing (CPTT) apparatus (Figure 11). The CPTT is a weldability test to evaluate the susceptibility to solidification cracking. The detailed procedure is described elsewhere [21]. Arc-melted button shaped samples are melted in a levitation coil and cast into pin shaped samples (Figure 11) using

copper molds of different lengths. The geometry of the mold and the shrinkage during solidification induces stresses in the solidifying pin, which can lead to cracking. The cast pin samples analyzed in this research were of 1 inch in length. This pin length was chosen because it is at the cracking threshold of the threshold for variant 4Ta0Mo (#5) and 2Ta4Mo (#4/6). Variant 4Ta4Mo (#6) had a slightly lower cracking threshold of 0.875 inch pin length, see Figure 1.

Figure 11: Cast pin tear test (CPTT) apparatus at The Ohio State University [20] (left), Cast pin samples of different lengths (right).

The second weldability test was the strain-to-fracture (STF) test. Again, all three filler metal variants in Table 4 were tested in the STF test in previous work [4]. The STF test evaluates the susceptibility for ductility dip cracking (DDC) by simulating the thermo-mechanical conditions in the heat affected zone (HAZ) of a weld in a Gleeble system (Figure 12). The test is done on dog bone samples, were the center of these

samples is melted with a GTA welding torch that creates a spot weld to realign the grain structure for testing uniformity. These samples are heated to the test temperature (usually 700-1150°C) and then a tensile strain of about 2-10% is applied. Details of the STF test are described elsewhere [22]. The STF samples analyzed in this work were strained to 9.7 % for variants 4Ta0Mo (#5) and 4Ta4Mo (#6) and 8.5 % for variant 2Ta4Mo (#4/6), all at a test temperature of 950 °C.

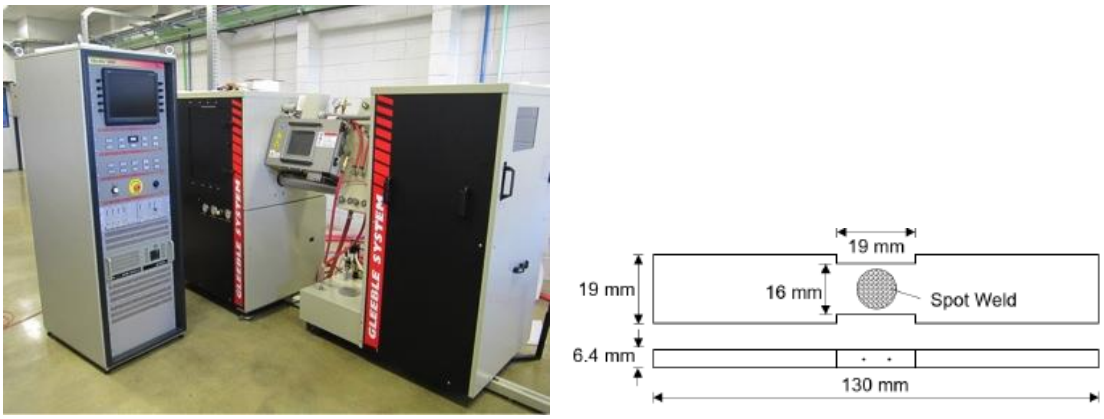

Figure 12: Greeble 3800 at The Ohio State University (left) and Dog-bone shaped sample for STF testing with GTA spot weld [4] (right)

4.2 Microstructural Characterization

4.2.1 Metallographic preparation

Cross sections of the button shaped as-melted samples were mounted in 1.5" Bakelite or KonductoMet, and were sanded down with sand papers in steps from 240 to 1200 grit. The samples were further polished with diamond paste with diamond extender

at stages of 6 micron, 3 micron, and 1 micron. Between each stage in polishing, the samples were cleaned in an ultrasonic bath and completely dried with a heat gun.

The overfill of the cast pin samples on the top and bottom of the shaft was removed before the samples were then mounted in Bakelite and then were ground down on a belt sander to approximately the middle of the cylindrical sample. The rest of the metallographic preparation was the same as is listed for the button samples. Both the buttons and the cast pin samples were etched with an electrolytic 10% chromic acid etch (CrO_3 in H_2O) for 4 s at 5 V. This etchant was used to see the precipitates that form on solidification in the interdendritic regions and solidification grain boundaries.

The gauge section of the STF samples was removed by mechanical sectioning. The samples were then mounted in KonductoMet so that the sample surface could be further analyzed in the scanning electron microscope (SEM). The polishing procedure was the same as for the button samples. The samples were then etched with an 10% electrolytic oxalic acid etch ($H_2C_2O_4$ in H_2O) for 4 s at 5 V. This etchant was used to bring out the grain boundaries (and any precipitates along the grain boundaries) for grain size analysis.

Analysis in the SEM was done on an FEI Apreo LoVac system at The Center for Electron Microscopy and Analysis (CEMAS) at The Ohio State University. Parameters used were a voltage of 20 kV, a current of 13 nA at a working distance of 10 mm. Images were taken at different magnifications to characterize the precipitation along the grain boundaries in the GTA spot weld of the STF samples.

4.2.2 Image Analysis

A light optical microscope (LOM) was used to take micrographs at different magnifications of the sample microstructures. The images of the buttons and the cast pin samples that were used to characterize phase formation upon solidification were taken at 1000x magnification. For the buttons there was a wide variety of pictures captured for general characterization of the solidification microstructure. For the cast pin samples, 15 images were taken for each sample near the top of the cast pin. This is the regions that solidifies last in the cast pin sample. For the STF samples, 4-6 images were taken from within the spot weld, schematically shown in Figure 13.

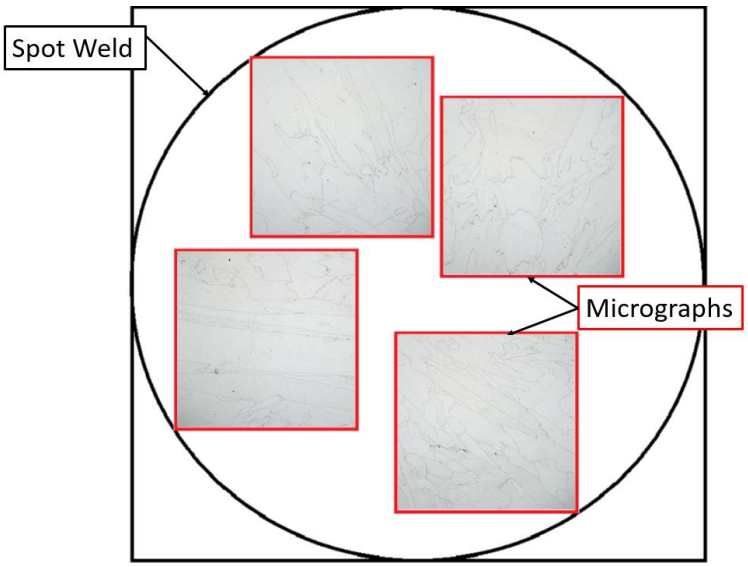

Figure 13: Schematic location of micrographs taken from STF samples.

MIPAR - Image analysis software was used to determine (1) fraction of second phases present in the solidification microstructure, (2) for grain size analysis, and (3) for determination of grain boundary tortuosity [23]. MIPAR can determine different colored

pixels from the surrounding pixels, so that small precipitates in the microstructure can be isolated and image analysis can be used to calculate the area fraction of the precipitates. The software was also used to measure the grain size in the GTA spot weld of the STF samples by segregating the interior of the grains. To analyze grain boundary tortuosity, the segregated interior of the grain was inverted so that only the grain boundaries were visible to measure the tortuosity. The use of two different tools in MIPAR, "Roughness" and "Curvature", were explored for measuring grain boundary tortuosity.

4.2.3 Hardness

The mounted button-shaped as melted samples were polished down to 3 micron in order to perform a hardness traverse with 75 number of indents across the center of the cross-section (Figure 14). The hardness was measured with the Vickers microhardness test (HV 0.1). Two hardness traverses were done on each sample at 2.5 mm and 3 mm from the bottom of the button.

Figure 14: Vickers microhardness indenter at The Ohio State University (left) and Mounted button sample with dashed lines indicating hardness traverses (right).

Chapter 5: Results and Discussion

5.1 Eutectic Phase Characterization

5.1.1 Characterization of Microstructure

The arc-melted button shaped samples exhibit a fully dendritic solidification microstructure. The interdendritic regions were more distinct in variant 4Ta4Mo (#6) as compared to variant 4Ta0Mo (#5). Interdendritic phase was observed in both as-melted materials, these interdendritic regions etch lighter due to a different composition (Figure 15). Primary MC precipitates form in a eutectic reaction at the end of solidification. They have been identified previously by other researchers as being Ta-rich carbides (TaC) [4]. These precipitates area the dark particles in the interdendritic region in Figure 15. New research shows that Mo- and Cr- rich Laves phase forms in the Mo containing variant 4Ta4Mo (#6) in addition to the eutectic carbides [24].

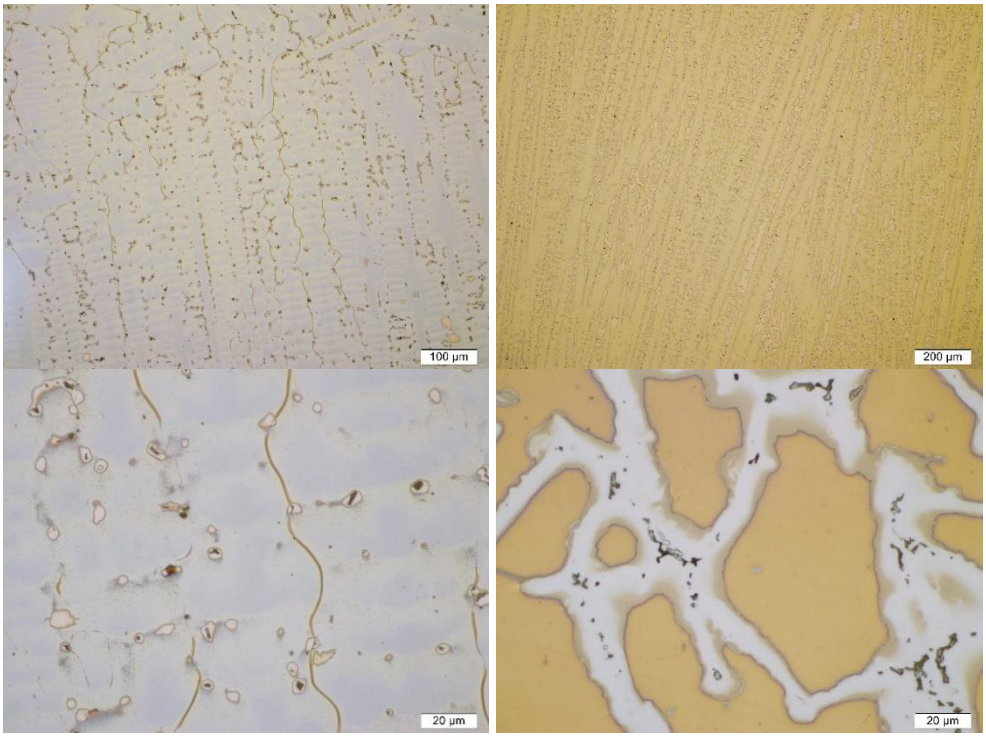

Figure 15: LOM images of solidification microstructure at two magnifications in arc melted button-shaped samples of filler metal variants 4Ta0Mo (#5) (left) and 4Ta4Mo (#5) (right)

5.1.2 Eutectic Phase Formation Analysis

Figure 16 shows LOM Micrographs of cast pin samples that have been processed for image analysis. The red colored areas indicate the interdendritic eutectic phase and were analyzed in MIPAR as area fraction of eutectic that forms at the end of solidification. The micrographs were taken from cast pin samples, so there could be a consistent cooling rate for both solidification microstructures. The eutectic comparison was done with variants 4Ta0Mo (#5) and 4Ta4Mo (#6) in order to determine if the addition of Mo had any effect on the eutectic formation.

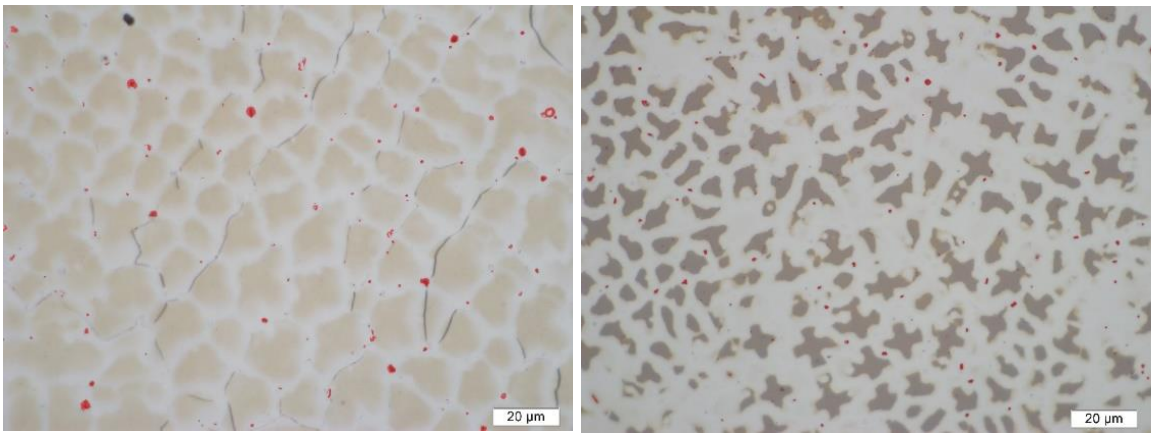

Figure 16: Image analysis of the microstructure of CPTT samples at 1000x magnification, the eutectic phase is highlighted in red, filler metal variant 4Ta0Mo (left), and 4Ta4Mo (right)

The results of the image analysis on the LOM micrographs is shown in Table 5. The results show that there was a slightly higher amount of eutectic phase measured in variant 4Ta0Mo (#5). However, using statistical analysis, it was determined that there was no significant difference in the amount of eutectic phase between both of the solidified filler metal variants. This seems to be in agreement with work done by Wheeling and Lippold [8] on Nb containing high Chromium filler metals, which did not find an increase in eutectic phase when Mo was added to the composition using qualitative comparison of LOM and SEM images and computational modeling in Thermo-Calc. However, the results of this study are in disagreement with previous work done by Fink et al. [4], which was done on the same filler metal variants studied in this research. This research found an increase in fraction eutectic when moly was added to Ta bearing 52XL-type filler metals.

Table 5: Results of fraction eutectic (%) measurements on LOM micrographs (15 images) of cast pin samples of filler metal variants 4Ta0Mo (#5) and 4Ta4Mo (#6). (Not statistically significant difference, p=0.20)

Variant	4Ta0Mo	4Ta4Mo
Average	**0.37**	**0.315**
Median	**0.346**	**0.309**
Minimum	**0.163**	**0.158**
Maximum	**0.597**	**0.471**
Standard Deviation	**0.119**	**0.105**

Figure 17 shows SEM images of the cast pin microstructures that were used for additional eutectic measurement. Images were taken from the same cast pins that were used for LOM analysis. The SEM images have a higher contrast of the eutectic phase as compared to the light optical micrographs, which makes it easier for the image processing software to detect and measure the eutectic phase fraction. However, the SEM images probe a slightly smaller area of the microstructure due to a higher magnification. The results of the image analysis in MIPAR are given in Table 6. In this analysis, a statistically significant difference was found between the amount of eutectic phase of filler metal variant 4Ta0Mo (#5) and 4Ta4Mo (#6). Additions of Mo clearly increased the fraction eutectic in the solidification microstructure in 4Ta4Mo (#6). This result is in agreement with previous work by Fink et al. [4]. The reason the initial image analysis on the LOM images may not reflect the actual fraction eutectic in the cast pin samples,

might be because of insufficient sample preparation which made it difficult for the image processing software to clearly distinguish the interdendritic eutectic phase. In any case, the measured phase fractions are very low, which makes it difficult to measure them accurately.

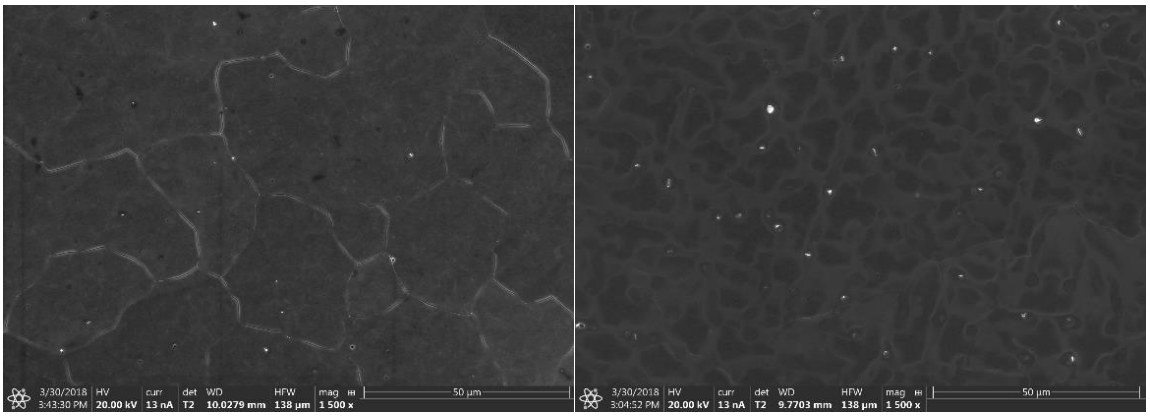

Figure 17: SEM images of cast pin microstructures of filler metal variant 4Ta0Mo (#5) (left), and 4Ta4Mo (#6) (right). Eutectic phase is seen as bright interdendritic particles.

Table 6: Area fraction (%) of SEM images (statistically significant difference of averages, p=0.00001)

Variant	**4Ta0Mo**	**4Ta4Mo**
Average	**0.047**	**0.119**
Median	**0.042**	**0.112**
Minimum	**0.036**	**0.090**
Maximum	**0.071**	**0.177**
Standard Deviation	**0.010**	**0.025**

5.2 Grain Size Analysis

Image analysis software MIPAR provides a mean of calculating the grain size in the GTA spot welds of the STF samples. LOM micrographs from different locations within the spot welds were used for the grain size measurements. Figure 18 shows micrographs form STF samples of all three filler metal variants before and after analyzed with MIPAR, where the software labels the grains and assigns different colors to each of the grains. Six micrographs for each variant were analyzed in Figure 18. There were two measurements done for each image: the first was to measure only the grains that did not border the exterior of the micrograph, i.e. were fully constrained within the image. The other one was to measure the grain size of all grains in the micrograph, including those that boarder the edge. The former was to get the true grain size for each image. The latter measurement was to determine how many very large grains there were in the spot welds as a function of filler metal composition, since most of the large grains bordered the edge of the micrograph. This is shown for example in Figure 19, where more than 4 micrographs were analyzed for each variant.

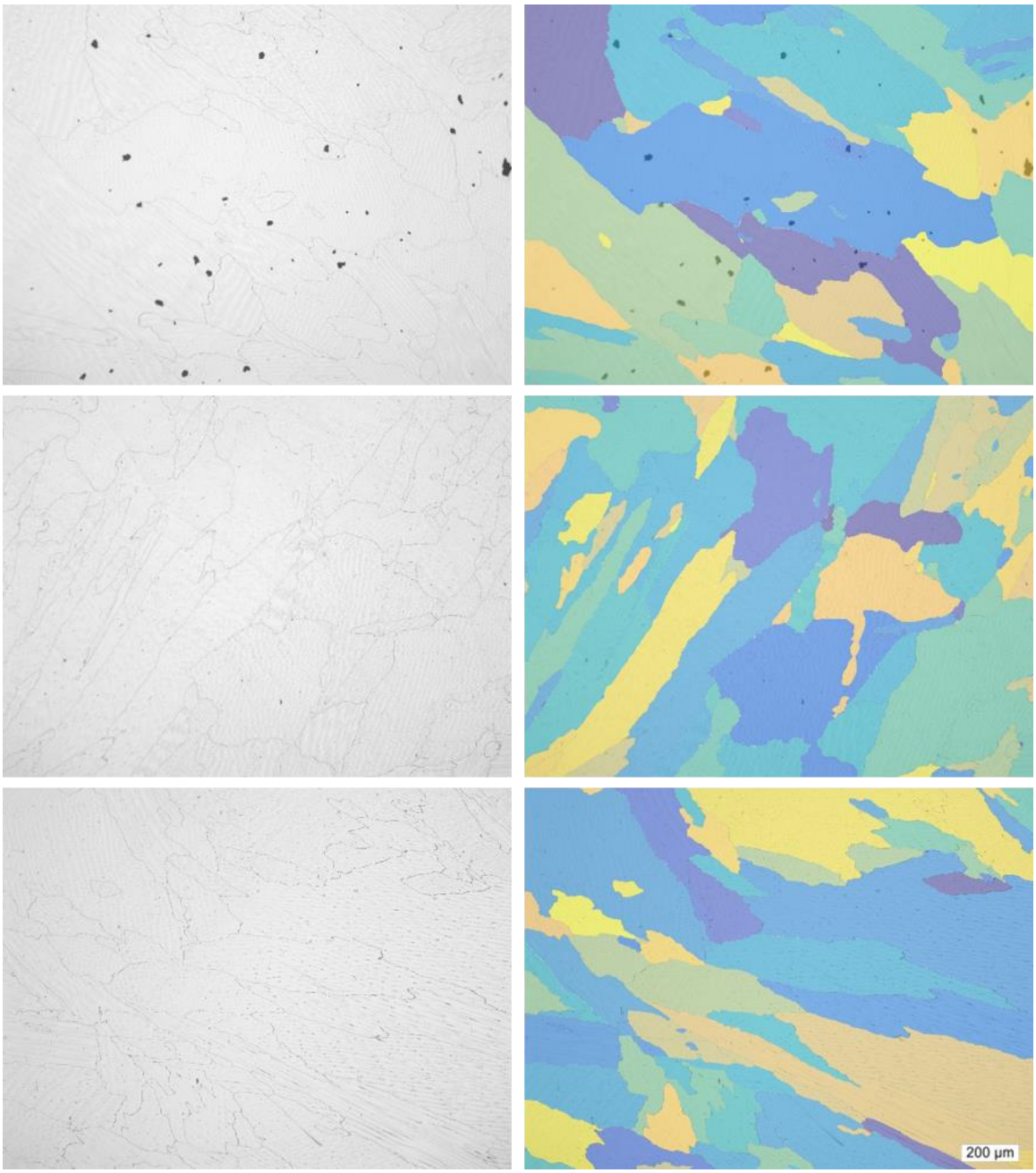

Figure 18: LOM images from GTA spot welds in STF samples processes with image analysis software MIPAR: Filler metal variant 2Ta4Mo (#4/6) (top), 4Ta0Mo (#5) (middle), and 4Ta4Mo (#6) (bottom). The left column shows the original micrographs, while the right column shows the processed images in MIPAR. Black spots in the top images were due to sample preparation.

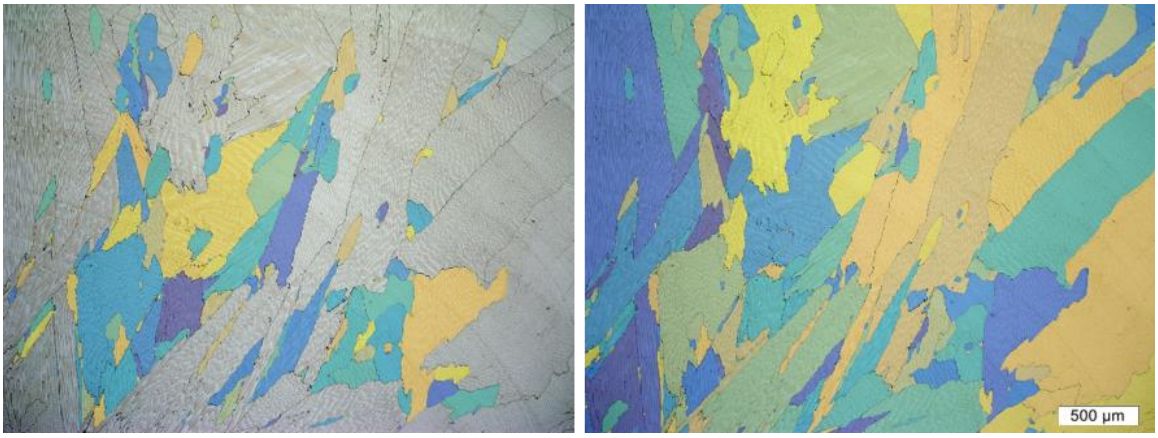

Figure 19: MIPAR image analysis of STF samples at 5x magnification filler metal variant 2Ta4Mo (#4/6)

Data for all micrographs of each filler metal variant were added up into cumulative histograms, see an example in Figure 20. The data was then divided by the number of micrographs analyzed for each variant to get average values for comparison of the three filler metals.

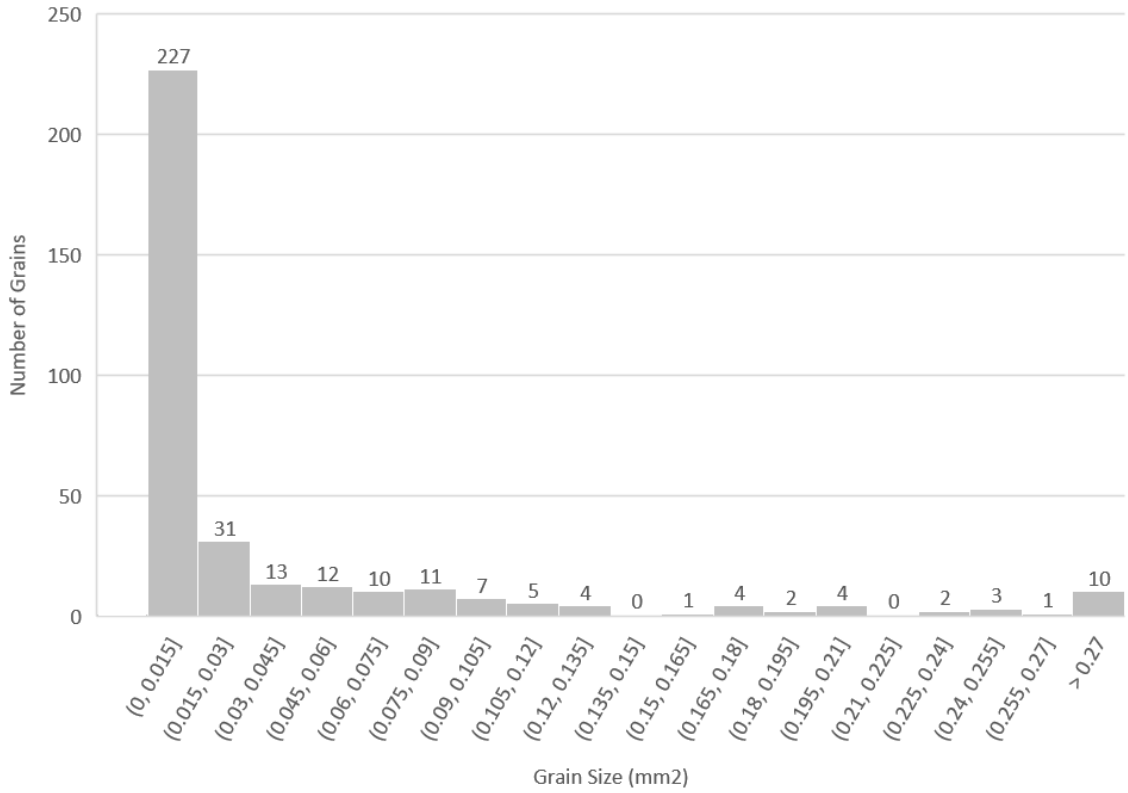

Figure 20: Cumulative histogram of all six micrographs of filler metal variant 2Ta4Mo (#4/6): Analysis was done with all grains in the micrograph (including the ones on the edges).

Figure 21 compares all three filler metals with regards to the number of grains in a specific grain size category. These results were obtained by considering all grains within a micrograph, not just the grains that were fully contained in the image.

From Figure 21 it appears that filler metal variant 4Ta4Mo (#6) has significant more smaller grains in the GTA spot weld of the STF samples as compared to the other two variants. Filler metals 4Ta0Mo (#5) and 2Ta4Mo (#4/6) have a similar grain size distribution in the spot welds. A smaller grain size would be beneficial for resistance to DDC, because strain would be better distributed in the microstructure due to much more

total grain boundary area. Less strain localization would happen at grain boundary triple points that could lead to DDC initiation by grain boundary sliding.

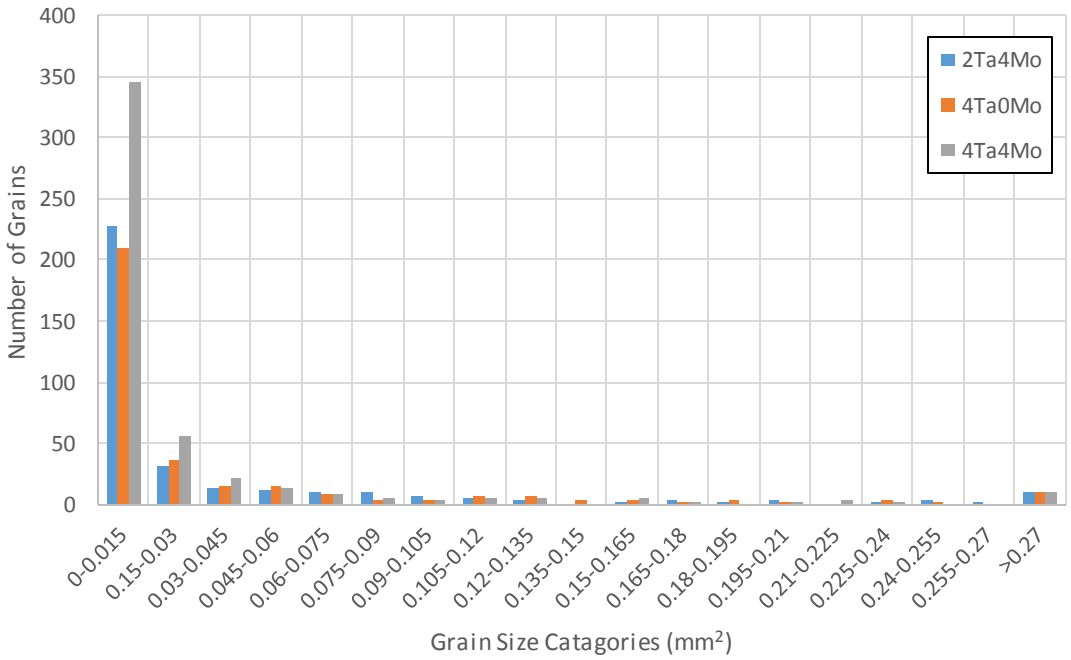

Figure 21: Comparison grain size of histograms for all three filler metals variants.

5.3 Analysis of Grain Boundary Tortuosity

5.3.1 MIPAR-Roughness

In the image analysis software MIPAR, there is a tool that is used to measure the roughness of a feature. An analysis was done in MIPAR to determine if this tool could be used to measure grain boundary tortuosity of weld metal microstructures. MIPAR's roughness tool measures the ratio of the convex hull to the area of each feature. The higher the roughness measurement the "rougher" the surface/boundary is. A value of 1

stands for a smooth grain boundary, meaning there is no tortuosity. A schematic of this measurement can be seen in Figure 22.

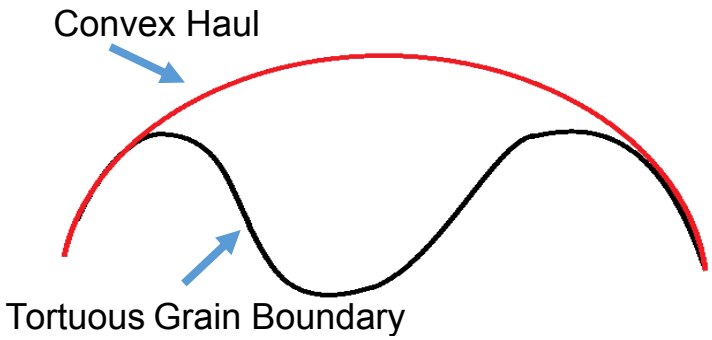

Figure 22: MIPAR grain boundary roughness schematic

The results are shown in Table 7. There is no statistically significant difference between the three filler metal variants. Also, the roughness tool gives false measurements of grain boundary tortuosity. A convex haul area can equal the area of a tortuous grain boundary, even if they are not the same, giving a false positive.

Table 7: Results for the measurement of roughness in MIPAR

Variant	**2Ta4Mo (#46)**	**4Ta0Mo (#5)**	**4Ta4Mo (#6)**
Mean	1.178092	1.198897	1.190357
Median	1.134479	1.159824	1.156259
Maximum	1.920349	2.377065	2.179946
Minimum	1.024007	1.025846	1.029501
Standard Deviation	0.15967	0.161655	0.145703

5.3.2 MIPAR-Curvature

Curvature is a feature in the image processing software MIPAR that was being evaluated for measuring the tortuosity of grain boundaries in the solidified weld metal microstructures. This is a local measure, where a circle is applied to each pixel and its immediate neighbors along a line (or grain boundary). At each pixel the tool measures the radius of that circle, as shown in Figure 23. A zero value corresponds to a straight line, since the curvature is 1/radius (μm). The higher the value in positive or negative direction, the more curvature, because the smaller the radius of the circle. Oxalic etched LOM micrographs of the GTA spot welded microstructure of the STF samples were used for the analysis in MIPAR. Four micrographs were analyzed for all filler metal variants.

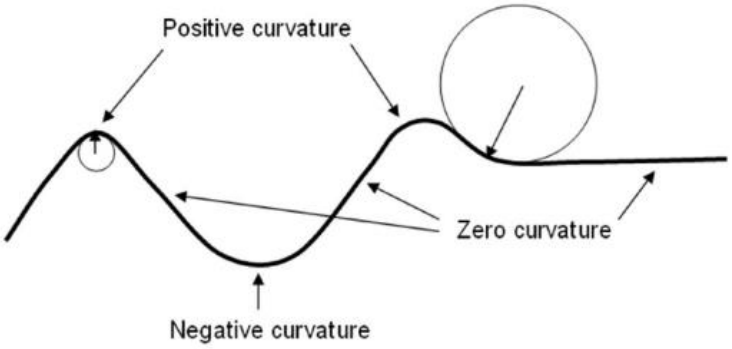

Figure 23: MIPAR local curvature measurement schematic [23].

From the analysis in MIPAR, histograms were obtained for all micrographs showing the number of pixels in the image with a certain curvature value. Figure 24 shows 3 histograms and their corresponding micrographs (processed in MIPAR) for each filler metal variant. The results in Table 8 show that the average curvature value is about the same for all three filler metal variants.

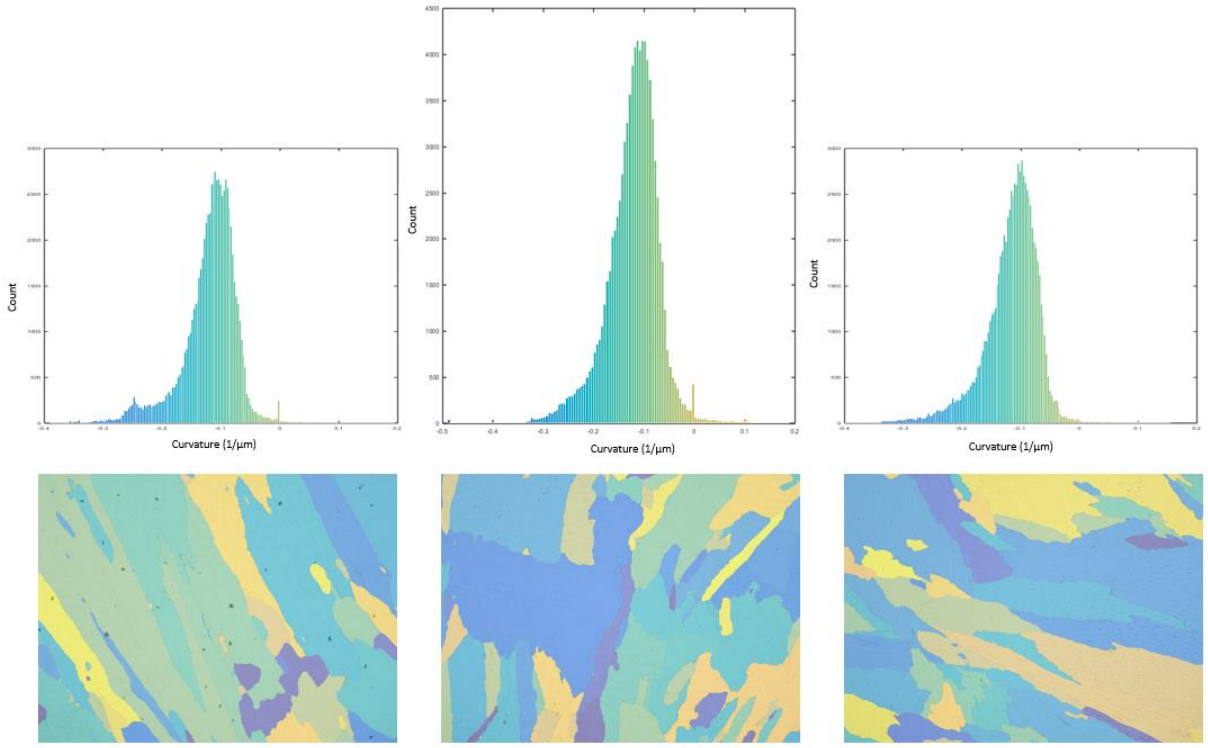

Figure 24: MIPAR image analysis of curvature on GTA spot weld microstructures of STF sample: Histograms measuring local curvature (top) and processed LOM micrographs (bottom). Sample composition from left to right 2Ta4Mo (#4/6), 4Ta0Mo (#5), and 4Ta4Mo (#6)

Table 8: Results from measurement of curvature in MIPAR.

Variant	**2Ta4Mo (#4/6)**	**4Ta0Mo (#5)**	**4Ta4Mo (#6)**
Average	-0.12	-0.126	-0.12
Median	-0.112	-0.119	-0.114
Minimum	-0.44	-0.485	-0.426
Maximum	0.23	0.222	0.21
Standard Deviation	0.052	0.053	0.046

From looking at the three micrographs in Figure 24, it seems that 4Ta0Mo (#5) has more tortuous grain boundaries than the other two filler metals. The MIPAR data from curvature was fed into MATLAB and further analyzed. All grain boundary pixels with a curvature (1/μm) less than -0.2 were separated (in all micrographs) and counted as fraction of total number of grain boundary pixels. This analysis was done for all filler metal variants. The results are shown in Table 9. Using this analysis, variant 4Ta0Mo (#5) has the highest fraction of grain boundary (GB) pixels with a curvature (1/μm) less than -0.2.

Table 9: MATLAB results of fraction of GB pixels less than -0.2 (1/μm)

Variant	**2Ta4Mo (#4/6)**	**4Ta0Mo (#5)**	**4Ta4Mo (#6)**
Number of pixels <-0.2	18239	26279	20186
Total number of GB pixels	239888	300900	350006
Fraction of pixels <-0.2	0.076031	0.087334	0.057673

Since MIPAR measures only the grain boundary pixels in the micrographs, from Table 9 it can be seen that the total number of GB pixels is highest in variant 4Ta4Mo (#6). This indicates that this weld metal has the finest grain structure, which is in agreement with the grain size measurements done in MIPAR (see previous section). Variant 2Ta4Mo (#4/6) has the largest grain size according to this analysis.

The results of grain boundary tortuosity using the curvature tool in MIPAR are somewhat contradictory to the DDC resistance measured using the STF test for the three filler metal variants. Variant 4Ta0Mo (#5) was measured to have the highest curvature of the grain boundaries, the results being in agreement to what is seen when visually comparing the micrographs of the three filler metal variants (Figure 24). However, variant 4Ta0Mo (#5) has the lowest cracking threshold in the STF test, meaning it was more susceptible to DDC than the other two variants. According to Ramirez and Lippold [13-14] a high grain boundary tortuosity should inhibit grain boundary sliding and therefor increase resistance to DDC. It has to be noted, that this analysis was done on only one STF samples per filler metal variant. The number of analyzed micrographs from the spot welded and STF tested microstructures was limited (4 micrographs each). Also, the observed tortuosity is much less than what was previously observed in Nb containing weld metals. This might be due to the much less amount of eutectic phase in the Ta containing 52M type filler metals. However, the Ta containing filler metals show a high DDC resistance, even though the grain boundary are not as tortuous. Grain boundary tortuosity might just be one factor affecting the DDC resistance in these filler metals. It might not be the primary reason why these filler metals show a good resistance to DDC.

5.4 Grain Boundary Precipitation

Analysis in the scanning electron microscope (SEM) was done in the GTA spot weld of the STF samples to look at differences in grain boundary precipitation between the three filler metal variants. Figure 25 shows SEM images of the observed precipitation at the grain boundaries in all three materials. Several grain boundaries were analyzed in

the SEM and the images in Figure 25 are representative of the majority of grain boundaries in each microstructure. However, the sampling in the SEM is due to the high magnification relatively small. Continuous grain boundary precipitation was observed in all three microstructures, and at higher magnification distinct particles can be made out. Based on previous research [7], the precipitates along the grain boundaries were identified as $M_{23}C_6$, in which M is primarily Chromium (Cr). These carbides were reported to form below the melting temperature at 2077 °F (~1136 °C) in the solid-state. This temperature is lower than the test temperature in the STF test (950 °C), this indicates that these carbides formed during the cooling down from the solidified GTA spot weld, not during the actual STF testing. The high temperatures during the STF test might have caused coarsening of these carbides, though the high temperature exposure in the STF test is probably less than a minute.

From the SEM images in Figure 25 it appears that in filler metal variant 4Ta0Mo (#5), the carbide particles along the grain boundaries are coarser as compared to the other two Mo- bearing variants. Given the coarser precipitates in variant 4Ta0Mo (#5), this could have an effect on the DDC resistance in the STF test. Coarser particles could increase DDC susceptibility due to an increase in strain concentration at the precipitates along the grain boundaries, Figure 7. This strain localization could lead to void formation and subsequent crack initiation. Filler metal variant 4Ta0Mo (#5) actually has the lowest cracking threshold in the STF test (Figure 9), which might support this reasoning. Finer carbide precipitates in variants 2Ta4Mo (#4/6) and 4Ta4Mo (#6) could in contrast provide a mechanical locking effect if they are finely distributed along the grain

boundaries, as seen in Figure 25. This mechanical locking would mitigate grain boundary sliding and cause a higher resistance to DDC.

Besides the grain boundary precipitation, very small precipitates can be seen in the areas next to the grain boundary in Figure 25. These are probably also $M_{23}C_6$ carbides that formed on cooling, in the interdendritic regions of the solidification microstructure. These areas are colored lighter than the dendritic areas due to a different composition.

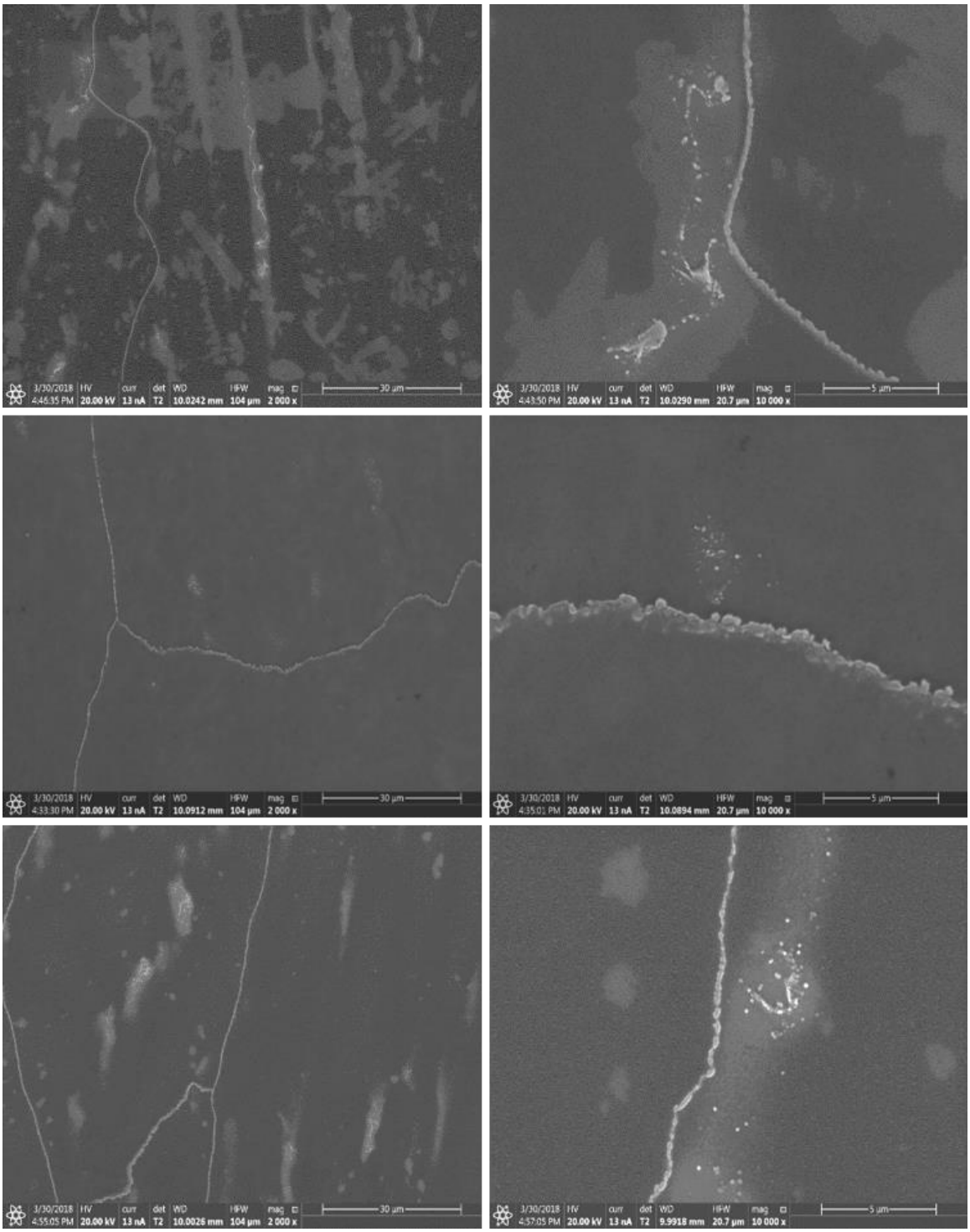

Figure 25: SEM Images in two magnification of grain boundary precipitation in GTA spot weld of STF samples: Filler metal variant 4Ta4Mo (#6) (top), 4Ta0Mo (#5) (middle), and 2Ta4Mo (#4/6) (bottom).

5.5 Solid-Solution Strengthening

Microhardness testing is comparably proportionate to the strength of a material. Mo is added to high chromium nickel-base alloys for solid-solution strengthening. Hardness measurements were made on the as-melted button shaped samples for all three filler metal variations. The results are shown in Figure 26 and Table 10.

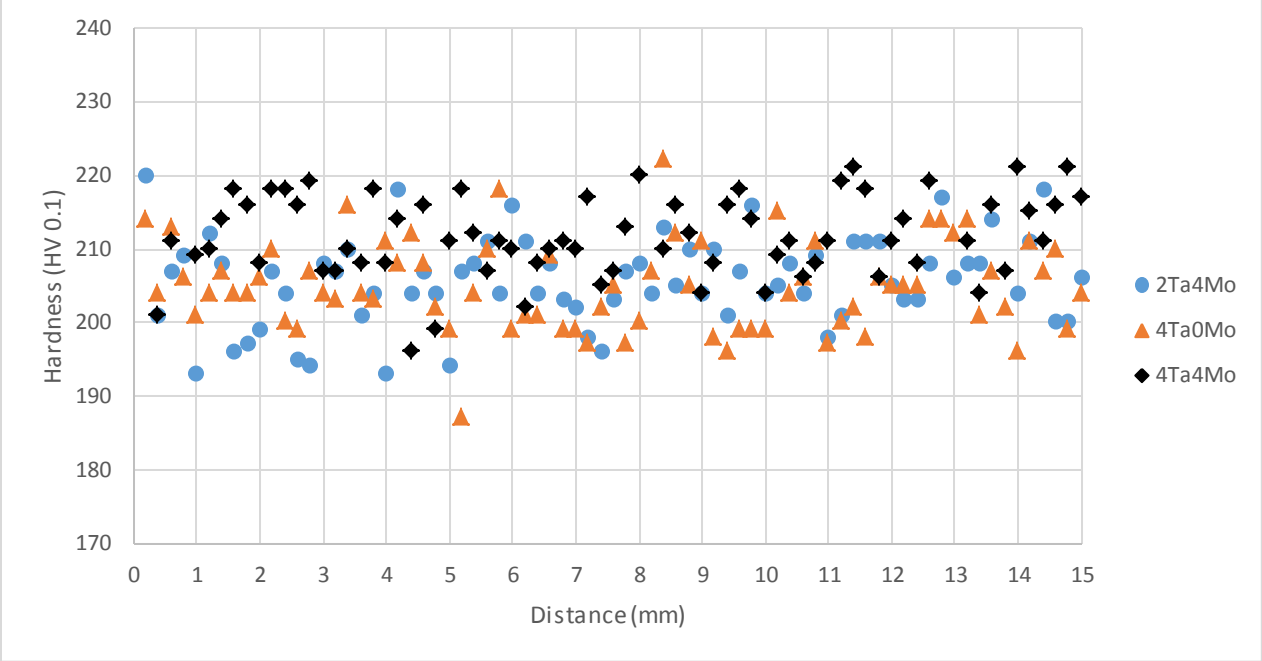

Figure 26: Micro hardness traverses on button shaped arc-melted samples

Table 10: Results of micro-hardness measurements (Vickers HV0.1) on as-melted button shaped samples of filler metal variants 4Ta0Mo (#5), 4Ta4Mo (#6) and 2Ta4Mo (#4/6). (Statistically significant difference, p=.000083)

Variant	**2Ta4Mo (#4/6)**	**4Ta0Mo (#5)**	**4Ta4Mo (#6)**
Average	206.3	204.9	210.7
Median	206	204	211
Minimum	193	187	142
Maximum	251	222	221
Standard Deviation	7.92	6.09	9.87

The sample with the highest hardness in the as-solidified microstructure is filler metal variant 4Ta4Mo (#6), which has the highest amount of alloying elements due to additions of Ta and Mo. Its hardness is higher than variant 2Ta4Mo (#4/6), which indicates that Ta also has a solid-solution strengthening effect in these filler metals. The obtained hardness ranking between the three variants is the same as in previous work by Fink et al. [4], which measured hardness on solidified cast pin samples.

From the hardness results, it can be concluded that both Mo and Ta have a solid-solution strengthening effect in these filler metals. These elements would therefore increase the strength of the grain interiors. During deformation at elevated temperatures, the strengthened grains would be less likely to deform, which could impose higher stresses on the grain boundaries. Grain boundary sliding is caused by the yielding of the material on the grain boundary. Therefore, additions of Ta and Mo could potentially

increase the susceptibility for DDC. However, the STF test showed that the highly alloyed filler metal variants have a higher cracking threshold, see Figure 9.

Chapter 6: Summary and Conclusions

This study was done to investigate the effect of Mo additions in high-chromium nickel-base filler metals on DDC resistance. The analysis was done on three variants of a newly developed Ta containing 52M type filler metal (52XL) with different addition of Ta and Mo. The following conclusions can be drawn from this work:

1. Image analysis to determine eutectic phase fraction was done using LOM and SEM images. Analysis on LOM images did not show a statistically significant difference between the filler metal variants without Mo addition (4Ta0Mo - #5) and with added Mo (4Ta4Mo - #6). However, image analysis on SEM images showed a significant increase in eutectic phase fraction when Mo was added to the filler metal. The latter seems in good agreement with results previously published on the same test materials.
2. The filler metal variant with Mo additions (4Ta4Mo - #6) of the STF samples has more smaller grains in the GTA spot welded microstructure than the other two variants. This might contribute to the higher DDC resistance of this variant in the STF test. The reason for the smaller grain size of variant 4Ta4Mo (#6) is unclear.

3. For grain size analysis in image analysis software MIPAR, the magnification of the LOM micrographs should be chosen so that they contain a high enough number of grains. Oxalic etch works well for Nickel-base weld metals to bring out grain boundaries for grain size analysis.

4. The roughness tool in MIPAR does not seem to be valuable to measure grain boundary tortuosity in the weld metals. The curvature tool might be useful in future projects to evaluate grain boundary tortuosity. In this study the results were in agreement to visual observation, meaning the curvature value was higher in the microstructure which seemed visually to be the most tortuous. Future analysis on other weld metals should be done to confirm the usefulness of this tool in MIPAR.

5. Filler metal variant 4Ta0Mo (#5) was measured to have the highest curvature of the weld metal grain boundaries. This was in agreement with the visual comparison of micrographs of all three filler metal variants. However, variant 4Ta0Mo (#5) has the lowest resistance to DDC as previously measured using the STF test. Also, all Ta bearing variants had a much lower grain boundary tortuosity than was reported in the literature for Nb containing FM 52. Given the relatively high DDC resistance of all Ta bearing variants, this indicates that grain boundary tortuosity might not be the only factor contributing to a high DDC resistance in these filler metals.

6. Using SEM analysis, $M_{23}C_6$ precipitates were observed along the solidification grain boundaries in the GTA spot welded microstructures of the

STF samples of all three Ta bearing filler metal variants. These carbides form in solid-state after solidification. Their high solvus temperature indicates that they formed during the GTA spot welding prior to STF testing in the samples. Thus, these carbides were in the microstructure when the samples were subjected to strain at 950 °C in the STF test, and might play a role for DDC resistance in the Ta bearing filler metals. It was observed that in variant 4Ta0Mo (#5) the grain boundary carbides seem to be larger as compared to the other filler metal variants. According to the literature, coarse particles along the grain boundaries could impose localized strains that lead to void formation and DDC. This could potentially explain the lower cracking threshold of variant 4Ta0Mo (#5) in the STF test. In contrast, variants 2Ta4Mo (#4/6) and 4Ta4Mo (#6) have smaller sized particles continuously distributed along the grain boundaries. These finer carbides could have a mechanical locking effect on grain boundary sliding and therefore could increase DDC resistance. This is again in good agreement with their higher cracking threshold in the STF test.

7. It was shown, that both Mo and Ta have a solid-solution strengthening effect on FM 52XL. This would strengthen the interior of grains as compared to the strength at the grain boundaries, which could potentially have a detrimental effect on DDC, since the deformation would be shifted from the grain interior to the grain boundaries. However, previous STF test results show that the cracking threshold of variants with Ta and Mo additions is higher as compared

to the variants without Mo additions. The effect of the solid-strengthening in relation to DDC is still unclear.

Bibliography

1. "Stress Corrosion Cracking in Light Water Reactors: Good Practices and Lessons Learned. International Atomic Energy Agency", No. NP-T-3.13, 2011.
2. Noecker II, F. F., and DuPont, J. N. 2009. "Metallurgical investigation into ductility dip cracking in Ni-based alloys: Part I." Welding Journal 88(1): 7-s to 20-s.
3. J. N. DuPont, C. V. Robino, and A. R. Marder, "Solidification and Weldability of Nb-Bearing Superalloys," Weld. J. Weld. Res. Suppl., vol. 77, p. 417s–431s, 1998.
4. Carolin Fink, John C. Lippold, Adam T. Hope, and Steven McCracken, "Elevated Temperature Cracking Resistance of Ta-Bearing High Chromium Ni-Base Filler Metals." in ASME, 2017, p. V06BT06A029.
5. Ramirez AJ, Lippold JC. High temperature cracking in nickel-base weld metal, Part 2: Insight into the mechanism. Mater Sci Eng A 2004; 380:245–258.
6. Lippold, J. C. and Nissley, N. E. 2008. Ductility dip cracking in high - Cr Ni – base filler metals, Hot Cracking Phenomena in Welds II, Springer, ISBN 978 - 3 - 540 -78627 - 6, pp. 409 – 426.

7. Zhang, Xu (2016). "Effect of Nb and Mo on the Microstructure, Mechanical Properties and Ductility-Dip Cracking of Ni-Cr-Fe Weld Metals". Acta metallurgica sinica: English letters (1006-7191), 29 (10), p. 928.
8. Wheeling, R. A., Lippold J. C., 2016. "Characterization of weld metal microstructure in a Ni-30Cr Alloy with additions of niobium and molybdenum". Materials Characterization.
9. Wheeling, R. A., Lippold J. C., 2017. "Effect of composition on grain boundary wetting characteristics in Ni-30Cr weld metal". International Institute of Welding, Weld World.
10. Lippold, John C., 2009. "Ch 4: Solid-State Cracking." Welding Metallurgy and Weldability. John Wiley & Sons, 2015.
11. Bengough GD. "A study of the properties of alloys at high temperatures". J Inst Metals 1912; VII:123–174.
12. Rhines FN, Wray PJ. Investigation of the intermediate temperature ductility minimum in metals. Trans ASM 1961;54:117–128.
13. Ramirez AJ, Lippold JC. High temperature cracking in nickel-base weld metal, Part 2: Insight into the mechanism. Mater Sci Eng A 2004;380:245–258.
14. Ramirez AJ, Lippold JC. New insight into the mechanism of ductility dip cracking in Ni-base weld metals. In: Böllinghaus T, Herold H, editors. Hot Cracking Phenomena in Welds. Berlin/Heidelberg: Springer; 2005. p 19–41.

15. Collins , M. G. and Lippold, J. C. 2003 . An investigation of ductility - dip cracking in nickel - based filler metals — Part I, Welding Journal, 82 (10): 288s – 295s.
16. Collins, M.G., Ramirez, A. J., Lippold, J. C., 2004. An Investigation of Ductility-Dip Cracking in Nickel-Based Weld Metals - Part III, Welding Journal, 83 (2): 39s - 49s.
17. Dupont JN, Lippold JC, Kiser SD. Welding Metallurgy and Weldability of Nickel Base Alloys. Hoboken, NJ: Wiley and Sons, Inc; 2009. p 138–142.
18. Young, G.A, Capobianco, T.E, Penik, M.A, Morris, B. W., and McGee, J. J. 2008. The mechanism for ductility dip cracking in nickel - chromium alloys, Welding Journal, 87 (2): 31s – 43s.
19. Hope, Adam T., and John C. Lippold. "Development and Testing of a High-Chromium, Ni-Based Filler Metal Resistant to Ductility Dip Cracking and Solidification Cracking." SpringerLink, Springer Berlin Heidelberg, 12 Jan. 2017.
20. E. Przybylowicz, Master's Thesis: Weldability Evaluation of High-Cr Ni-base Filler Metals using the Cast Pin Tear Test, Columbus, OH, 2015.
21. B. T. Alexandrov and J. C. Lippold, "Use of the cast pin tear test to study solidification cracking," Weld. World, vol. 57, no. 5, pp. 635–648, Sep. 2013.
22. N.E. Nissley and J.C. Lippold: Weld. J., 2003, vol. 82, p. 355s–364s.
23. "Image Analysis Software." MIPAR, MIPAR, www.mipar.us/.

24. Li, C.-H.; Shao, M.; Jinschek, J.; Fink, C.; Lippold, J.C.:TEM Investigation on Eutectic Phase Formation in Ni-30Cr Filler Metal 52XL, Microscopy and Microanalysis, Baltimore, MD, August 5-9, 2018 (Extended Abstract).